

Measurement of proton electromagnetic form factors in the time-like region using initial state radiation at BESIII

M. Ablikim¹, M. N. Achasov^{10,c}, P. Adlarson⁶⁷, S. Ahmed¹⁵, M. Albrecht⁴, R. Aliberti²⁸, A. Amoroso^{66A,66C}, M. R. An³², Q. An^{63,49}, X. H. Bai⁵⁷, Y. Bai⁴⁸, O. Bakina²⁹, R. Baldini Ferroli^{23A}, I. Balossino^{24A}, Y. Ban^{38,k}, K. Begzsuren²⁶, N. Berger²⁸, M. Bertani^{23A}, D. Bettoni^{24A}, F. Bianchi^{66A,66C}, J. Bloms⁶⁰, A. Bortone^{66A,66C}, I. Boyko²⁹, R. A. Briere⁵, H. Cai⁶⁸, X. Cai^{1,49}, A. Calcaterra^{23A}, G. F. Cao^{1,54}, N. Cao^{1,54}, S. A. Cetin^{53A}, J. F. Chang^{1,49}, W. L. Chang^{1,54}, G. Chelkov^{29,b}, D. Y. Chen⁶, G. Chen¹, H. S. Chen^{1,54}, M. L. Chen^{1,49}, S. J. Chen³⁵, X. R. Chen²⁵, Y. B. Chen^{1,49}, Z. J. Chen^{20,l}, W. S. Cheng^{66C}, G. Cibinetto^{24A}, F. Cossio^{66C}, X. F. Cui³⁶, H. L. Dai^{1,49}, X. C. Dai^{1,54}, A. Dbeysy¹⁵, R. E. de Boer⁴, D. Dedovich²⁹, Z. Y. Deng¹, A. Denig²⁸, I. Denysenko²⁹, M. Destefanis^{66A,66C}, F. De Mori^{66A,66C}, Y. Ding³³, C. Dong³⁶, J. Dong^{1,49}, L. Y. Dong^{1,54}, M. Y. Dong^{1,49,54}, X. Dong⁶⁸, S. X. Du⁷¹, Y. L. Fan⁶⁸, J. Fang^{1,49}, S. S. Fang^{1,54}, Y. Fang¹, R. Farinelli^{24A}, L. Fava^{66B,66C}, F. Feldbauer⁴, G. Felici^{23A}, C. Q. Feng^{63,49}, J. H. Feng⁵⁰, M. Fritsch⁴, C. D. Fu¹, Y. Gao^{63,49}, Y. Gao^{38,k}, Y. Gao⁶⁴, Y. G. Gao⁶, I. Garzia^{24A,24B}, P. T. Ge⁶⁸, C. Geng⁵⁰, E. M. Gersabeck⁵⁸, A. Gilman⁶¹, K. Goetzen¹¹, L. Gong³³, W. X. Gong^{1,49}, W. Gradl²⁸, M. Greco^{66A,66C}, L. M. Gu³⁵, M. H. Gu^{1,49}, S. Gu², Y. T. Gu¹³, C. Y. Guan^{1,54}, A. Q. Guo²², L. B. Guo³⁴, R. P. Guo⁴⁰, Y. P. Guo^{9,h}, A. Guskov^{29,b}, T. T. Han⁴¹, W. Y. Han³², X. Q. Hao¹⁶, F. A. Harris⁵⁶, N. Hüsken⁶⁰, K. L. He^{1,54}, F. H. Heinsius⁴, C. H. Heinz²⁸, T. Held⁴, Y. K. Heng^{1,49,54}, C. Herold⁵¹, M. Himmelreich^{11,f}, T. Holtmann⁴, G. Y. Hou^{1,54}, Y. R. Hou⁵⁴, Z. L. Hou¹, H. M. Hu^{1,54}, J. F. Hu^{47,m}, T. Hu^{1,49,54}, Y. Hu¹, G. S. Huang^{63,49}, L. Q. Huang⁶⁴, X. T. Huang⁴¹, Y. P. Huang¹, Z. Huang^{38,k}, T. Hussain⁶⁵, W. Ikegami Andersson⁶⁷, W. Imoehl²², M. Irshad^{63,49}, S. Jaeger⁴, S. Janchiv^{26,j}, Q. Ji¹, Q. P. Ji¹⁶, X. B. Ji^{1,54}, X. L. Ji^{1,49}, Y. Y. Ji⁴¹, H. B. Jiang⁴¹, X. S. Jiang^{1,49,54}, J. B. Jiao⁴¹, Z. Jiao¹⁸, S. Jin³⁵, Y. Jin⁵⁷, M. Q. Jing^{1,54}, T. Johansson⁶⁷, N. Kalantar-Nayestanaki⁵⁵, X. S. Kang³³, R. Kappert⁵⁵, M. Kavatsyuk⁵⁵, B. C. Ke^{43,1}, I. K. Keshk⁴, A. Khoukaz⁶⁰, P. Kiese²⁸, R. Kiuchi¹, R. Kliemt¹¹, L. Koch³⁰, O. B. Kolcu^{53A,e}, B. Kopf⁴, M. Kuemmel⁴, M. Kuessner⁴, A. Kupsc⁶⁷, M. G. Kurth^{1,54}, W. Kühn³⁰, J. J. Lane⁵⁸, J. S. Lange³⁰, P. Larin¹⁵, A. Lavania²¹, L. Lavezzi^{66A,66C}, Z. H. Lei^{63,49}, H. Leithoff²⁸, M. Lellmann²⁸, T. Lenz²⁸, C. Li³⁹, C. H. Li³², Cheng Li^{63,49}, D. M. Li⁷¹, F. Li^{1,49}, G. Li¹, H. Li⁴³, H. Li^{63,49}, H. B. Li^{1,54}, H. J. Li^{9,h}, J. L. Li⁴¹, J. Q. Li⁴, J. S. Li⁵⁰, Ke Li¹, L. K. Li¹, Lei Li³, P. R. Li³¹, S. Y. Li⁵², W. D. Li^{1,54}, W. G. Li¹, X. H. Li^{63,49}, X. L. Li⁴¹, Xiaoyu Li^{1,54}, Z. Y. Li⁵⁰, H. Liang^{1,54}, H. Liang^{63,49}, H. Liang²⁷, Y. F. Liang⁴⁵, Y. T. Liang²⁵, G. R. Liao¹², L. Z. Liao^{1,54}, J. Libby²¹, C. X. Lin⁵⁰, D. X. Lin^{15,n}, B. J. Liu¹, C. X. Liu¹, D. Liu^{63,49}, F. H. Liu⁴⁴, Fang Liu¹, Feng Liu⁶, H. B. Liu¹³, H. M. Liu^{1,54}, Huanhuan Liu¹, Huihui Liu¹⁷, J. B. Liu^{63,49}, J. L. Liu⁶⁴, J. Y. Liu^{1,54}, K. Liu¹, K. Y. Liu³³, L. Liu^{63,49}, M. H. Liu^{9,h}, P. L. Liu¹, Q. Liu⁶⁸, Q. Liu⁵⁴, S. B. Liu^{63,49}, Shuai Liu⁴⁶, T. Liu^{1,54}, W. M. Liu^{63,49}, X. Liu³¹, Y. Liu³¹, Y. B. Liu³⁶, Z. A. Liu^{1,49,54}, Z. Q. Liu⁴¹, X. C. Lou^{1,49,54}, F. X. Lu¹⁶, F. X. Lu⁵⁰, H. J. Lu¹⁸, J. D. Lu^{1,54}, J. G. Lu^{1,49}, X. L. Lu¹, Y. Lu¹, Y. P. Lu^{1,49}, C. L. Luo³⁴, M. X. Luo⁷⁰, P. W. Luo⁵⁰, T. Luo^{9,h}, X. L. Luo^{1,49}, S. Lusso^{66C}, X. R. Lyu⁵⁴, F. C. Ma³³, H. L. Ma¹, L. L. Ma⁴¹, M. M. Ma^{1,54}, Q. M. Ma¹, R. Q. Ma^{1,54}, R. T. Ma⁵⁴, X. X. Ma^{1,54}, X. Y. Ma^{1,49}, F. E. Maas¹⁵, M. Maggiora^{66A,66C}, S. Maldaner⁴, S. Malde⁶¹, Q. A. Malik⁶⁵, A. Mangoni^{23B}, Y. J. Mao^{38,k}, Z. P. Mao¹, S. Marcello^{66A,66C}, Z. X. Meng⁵⁷, J. G. Messchendorp⁵⁵, G. Mezzadri^{24A}, T. J. Min³⁵, R. E. Mitchell²², X. H. Mo^{1,49,54}, Y. J. Mo⁶, N. Yu. Muchnoi^{10,c}, H. Muramatsu⁵⁹, S. Nakhoul^{11,f}, Y. Nefedov²⁹, F. Nerling^{11,f}, I. B. Nikolaev^{10,c}, Z. Ning^{1,49}, S. Nisar^{8,i}, S. L. Olsen⁵⁴, Q. Ouyang^{1,49,54}, S. Pacetti^{23B,23C}, X. Pan^{9,h}, Y. Pan⁵⁸, A. Pathak¹, P. Patteri^{23A}, M. Pelizaeus⁴, H. P. Peng^{63,49}, K. Peters^{11,f}, J. Pettersson⁶⁷, J. L. Ping³⁴, R. G. Ping^{1,54}, R. Poling⁵⁹, V. Prasad^{63,49}, H. Qi^{63,49}, H. R. Qi⁵², K. H. Qi²⁵, M. Qi³⁵, T. Y. Qi², T. Y. Qi⁹, S. Qian^{1,49}, W. B. Qian⁵⁴, Z. Qian⁵⁰, C. F. Qiao⁵⁴, L. Q. Qin¹², X. P. Qin⁹, X. S. Qin⁴¹, Z. H. Qin^{1,49}, J. F. Qiu¹, S. Q. Qu³⁶, K. H. Rashid⁶⁵, K. Ravindran²¹, C. F. Redmer²⁸, A. Rivetti^{66C}, V. Rodin⁵⁵, M. Rolo^{66C}, G. Rong^{1,54}, Ch. Rosner¹⁵, M. Rump⁶⁰, H. S. Sang⁶³, A. Sarantsev^{29,d}, Y. Schelhaas²⁸, C. Schnier⁴, K. Schoenning⁶⁷, M. Scodeggio^{24A,24B}, D. C. Shan⁴⁶, W. Shan¹⁹, X. Y. Shan^{63,49}, J. F. Shangguan⁴⁶, M. Shao^{63,49}, C. P. Shen⁹, H. F. Shen^{1,54}, P. X. Shen³⁶, X. Y. Shen^{1,54}, H. C. Shi^{63,49}, R. S. Shi^{1,54}, X. Shi^{1,49}, X. D. Shi^{63,49}, J. J. Song⁴¹, W. M. Song^{27,1}, Y. X. Song^{38,k}, S. Sosio^{66A,66C}, S. Spataro^{66A,66C}, K. X. Su⁶⁸, P. P. Su⁴⁶, F. F. Sui⁴¹, G. X. Sun¹, H. K. Sun¹,

J. F. Sun¹⁶, L. Sun⁶⁸, S. S. Sun^{1,54}, T. Sun^{1,54}, W. Y. Sun³⁴, W. Y. Sun²⁷, X. Sun^{20,l}, Y. J. Sun^{63,49}, Y. K. Sun^{63,49},
Y. Z. Sun¹, Z. T. Sun¹, Y. H. Tan⁶⁸, Y. X. Tan^{63,49}, C. J. Tang⁴⁵, G. Y. Tang¹, J. Tang⁵⁰, J. X. Teng^{63,49},
V. Thoren⁶⁷, W. H. Tian⁴³, I. Uman^{53B}, B. Wang¹, C. W. Wang³⁵, D. Y. Wang^{38,k}, H. J. Wang³¹, H. P. Wang^{1,54},
K. Wang^{1,49}, L. L. Wang¹, M. Wang⁴¹, M. Z. Wang^{38,k}, Meng Wang^{1,54}, W. Wang⁵⁰, W. H. Wang⁶⁸,
W. P. Wang^{63,49}, X. Wang^{38,k}, X. F. Wang³¹, X. L. Wang^{9,h}, Y. Wang^{63,49}, Y. Wang⁵⁰, Y. D. Wang³⁷,
Y. F. Wang^{1,49,54}, Y. Q. Wang¹, Y. Y. Wang³¹, Z. Wang^{1,49}, Z. Y. Wang¹, Ziyi Wang⁵⁴, Zongyuan Wang^{1,54},
D. H. Wei¹², P. Weidenkaff²⁸, F. Weidner⁶⁰, S. P. Wen¹, D. J. White⁵⁸, U. Wiedner⁴, G. Wilkinson⁶¹, M. Wolke⁶⁷,
L. Wollenberg⁴, J. F. Wu^{1,54}, L. H. Wu¹, L. J. Wu^{1,54}, X. Wu^{9,h}, Z. Wu^{1,49}, L. Xia^{63,49}, H. Xiao^{9,h}, S. Y. Xiao¹,
Z. J. Xiao³⁴, X. H. Xie^{38,k}, Y. G. Xie^{1,49}, Y. H. Xie⁶, T. Y. Xing^{1,54}, G. F. Xu¹, Q. J. Xu¹⁴, W. Xu^{1,54}, X. P. Xu⁴⁶,
Y. C. Xu⁵⁴, F. Yan^{9,h}, L. Yan^{9,h}, W. B. Yan^{63,49}, W. C. Yan⁷¹, Xu Yan⁴⁶, H. J. Yang^{42,g}, H. X. Yang¹, L. Yang⁴³,
S. L. Yang⁵⁴, Y. X. Yang¹², Yifan Yang^{1,54}, Zhi Yang²⁵, M. Ye^{1,49}, M. H. Ye⁷, J. H. Yin¹, Z. Y. You⁵⁰,
B. X. Yu^{1,49,54}, C. X. Yu³⁶, G. Yu^{1,54}, J. S. Yu^{20,l}, T. Yu⁶⁴, C. Z. Yuan^{1,54}, L. Yuan², X. Q. Yuan^{38,k}, Y. Yuan¹,
Z. Y. Yuan⁵⁰, C. X. Yue³², A. Yuncu^{53A,a}, A. A. Zafar⁶⁵, Zeng⁶, Y. Zeng^{20,l}, A. Q. Zhang¹, B. X. Zhang¹,
Guangyi Zhang¹⁶, H. Zhang⁶³, H. H. Zhang⁵⁰, H. H. Zhang²⁷, H. Y. Zhang^{1,49}, J. J. Zhang⁴³, J. L. Zhang⁶⁹,
J. Q. Zhang³⁴, J. W. Zhang^{1,49,54}, J. Y. Zhang¹, J. Z. Zhang^{1,54}, Jianyu Zhang^{1,54}, Jiawei Zhang^{1,54}, L. Q. Zhang⁵⁰,
Lei Zhang³⁵, S. Zhang⁵⁰, S. F. Zhang³⁵, Shulei Zhang^{20,l}, X. D. Zhang³⁷, X. Y. Zhang⁴¹, Y. Zhang⁶¹,
Y. H. Zhang^{1,49}, Y. T. Zhang^{63,49}, Yan Zhang^{63,49}, Yao Zhang¹, Yi Zhang^{9,h}, Z. H. Zhang⁶, Z. Y. Zhang⁶⁸,
G. Zhao¹, J. Zhao³², J. Y. Zhao^{1,54}, J. Z. Zhao^{1,49}, Lei Zhao^{63,49}, Ling Zhao¹, M. G. Zhao³⁶, Q. Zhao¹,
S. J. Zhao⁷¹, Y. B. Zhao^{1,49}, Y. X. Zhao²⁵, Z. G. Zhao^{63,49}, A. Zhemchugov^{29,b}, B. Zheng⁶⁴, J. P. Zheng^{1,49},
Y. Zheng^{38,k}, Y. H. Zheng⁵⁴, B. Zhong³⁴, C. Zhong⁶⁴, L. P. Zhou^{1,54}, Q. Zhou^{1,54}, X. Zhou⁶⁸, X. K. Zhou⁵⁴,
X. R. Zhou^{63,49}, A. N. Zhu^{1,54}, J. Zhu³⁶, K. Zhu¹, K. J. Zhu^{1,49,54}, S. H. Zhu⁶², T. J. Zhu⁶⁹, W. J. Zhu³⁶,
W. J. Zhu^{9,h}, Y. C. Zhu^{63,49}, Z. A. Zhu^{1,54}, B. S. Zou¹, J. H. Zou¹

(BESIII Collaboration)

¹ *Institute of High Energy Physics, Beijing 100049, People's Republic of China*

² *Beihang University, Beijing 100191, People's Republic of China*

³ *Beijing Institute of Petrochemical Technology, Beijing 102617, People's Republic of China*

⁴ *Bochum Ruhr-University, D-44780 Bochum, Germany*

⁵ *Carnegie Mellon University, Pittsburgh, Pennsylvania 15213, USA*

⁶ *Central China Normal University, Wuhan 430079, People's Republic of China*

⁷ *China Center of Advanced Science and Technology, Beijing 100190, People's Republic of China*

⁸ *COMSATS University Islamabad, Lahore Campus, Defence Road, Off Raiwind Road, 54000 Lahore, Pakistan*

⁹ *Fudan University, Shanghai 200443, People's Republic of China*

¹⁰ *G.I. Budker Institute of Nuclear Physics SB RAS (BINP), Novosibirsk 630090, Russia*

¹¹ *GSI Helmholtzcentre for Heavy Ion Research GmbH, D-64291 Darmstadt, Germany*

¹² *Guangxi Normal University, Guilin 541004, People's Republic of China*

¹³ *Guangxi University, Nanning 530004, People's Republic of China*

¹⁴ *Hangzhou Normal University, Hangzhou 310036, People's Republic of China*

¹⁵ *Helmholtz Institute Mainz, Staudinger Weg 18, D-55099 Mainz, Germany*

¹⁶ *Henan Normal University, Xinxiang 453007, People's Republic of China*

¹⁷ *Henan University of Science and Technology, Luoyang 471003, People's Republic of China*

¹⁸ *Huangshan College, Huangshan 245000, People's Republic of China*

¹⁹ *Hunan Normal University, Changsha 410081, People's Republic of China*

²⁰ *Hunan University, Changsha 410082, People's Republic of China*

²¹ *Indian Institute of Technology Madras, Chennai 600036, India*

²² *Indiana University, Bloomington, Indiana 47405, USA*

²³ *INFN Laboratori Nazionali di Frascati, (A)INFN Laboratori Nazionali di Frascati, I-00044, Frascati, Italy;*

(B)INFN Sezione di Perugia, I-06100, Perugia, Italy; (C)University of Perugia, I-06100, Perugia, Italy

- ²⁴ INFN Sezione di Ferrara, (A)INFN Sezione di Ferrara, I-44122, Ferrara, Italy; (B)University of Ferrara, I-44122, Ferrara, Italy
- ²⁵ Institute of Modern Physics, Lanzhou 730000, People's Republic of China
- ²⁶ Institute of Physics and Technology, Peace Ave. 54B, Ulaanbaatar 13330, Mongolia
- ²⁷ Jilin University, Changchun 130012, People's Republic of China
- ²⁸ Johannes Gutenberg University of Mainz, Johann-Joachim-Becher-Weg 45, D-55099 Mainz, Germany
- ²⁹ Joint Institute for Nuclear Research, 141980 Dubna, Moscow region, Russia
- ³⁰ Justus-Liebig-Universitaet Giessen, II. Physikalisches Institut, Heinrich-Buff-Ring 16, D-35392 Giessen, Germany
- ³¹ Lanzhou University, Lanzhou 730000, People's Republic of China
- ³² Liaoning Normal University, Dalian 116029, People's Republic of China
- ³³ Liaoning University, Shenyang 110036, People's Republic of China
- ³⁴ Nanjing Normal University, Nanjing 210023, People's Republic of China
- ³⁵ Nanjing University, Nanjing 210093, People's Republic of China
- ³⁶ Nankai University, Tianjin 300071, People's Republic of China
- ³⁷ North China Electric Power University, Beijing 102206, People's Republic of China
- ³⁸ Peking University, Beijing 100871, People's Republic of China
- ³⁹ Qufu Normal University, Qufu 273165, People's Republic of China
- ⁴⁰ Shandong Normal University, Jinan 250014, People's Republic of China
- ⁴¹ Shandong University, Jinan 250100, People's Republic of China
- ⁴² Shanghai Jiao Tong University, Shanghai 200240, People's Republic of China
- ⁴³ Shanxi Normal University, Linfen 041004, People's Republic of China
- ⁴⁴ Shanxi University, Taiyuan 030006, People's Republic of China
- ⁴⁵ Sichuan University, Chengdu 610064, People's Republic of China
- ⁴⁶ Soochow University, Suzhou 215006, People's Republic of China
- ⁴⁷ South China Normal University, Guangzhou 510006, People's Republic of China
- ⁴⁸ Southeast University, Nanjing 211100, People's Republic of China
- ⁴⁹ State Key Laboratory of Particle Detection and Electronics, Beijing 100049, Hefei 230026, People's Republic of China
- ⁵⁰ Sun Yat-Sen University, Guangzhou 510275, People's Republic of China
- ⁵¹ Suranaree University of Technology, University Avenue 111, Nakhon Ratchasima 30000, Thailand
- ⁵² Tsinghua University, Beijing 100084, People's Republic of China
- ⁵³ Turkish Accelerator Center Particle Factory Group, (A)Istanbul Bilgi University, 34060 Eyup, Istanbul, Turkey; (B)Near East University, Nicosia, North Cyprus, Mersin 10, Turkey
- ⁵⁴ University of Chinese Academy of Sciences, Beijing 100049, People's Republic of China
- ⁵⁵ University of Groningen, NL-9747 AA Groningen, The Netherlands
- ⁵⁶ University of Hawaii, Honolulu, Hawaii 96822, USA
- ⁵⁷ University of Jinan, Jinan 250022, People's Republic of China
- ⁵⁸ University of Manchester, Oxford Road, Manchester, M13 9PL, United Kingdom
- ⁵⁹ University of Minnesota, Minneapolis, Minnesota 55455, USA
- ⁶⁰ University of Muenster, Wilhelm-Klemm-Str. 9, 48149 Muenster, Germany
- ⁶¹ University of Oxford, Keble Rd, Oxford, UK OX13RH
- ⁶² University of Science and Technology Liaoning, Anshan 114051, People's Republic of China
- ⁶³ University of Science and Technology of China, Hefei 230026, People's Republic of China
- ⁶⁴ University of South China, Hengyang 421001, People's Republic of China
- ⁶⁵ University of the Punjab, Lahore-54590, Pakistan
- ⁶⁶ University of Turin and INFN, (A)University of Turin, I-10125, Turin, Italy; (B)University of Eastern Piedmont, I-15121, Alessandria, Italy; (C)INFN, I-10125, Turin, Italy
- ⁶⁷ Uppsala University, Box 516, SE-75120 Uppsala, Sweden

⁶⁸ Wuhan University, Wuhan 430072, People's Republic of China

⁶⁹ Xinyang Normal University, Xinyang 464000, People's Republic of China

⁷⁰ Zhejiang University, Hangzhou 310027, People's Republic of China

⁷¹ Zhengzhou University, Zhengzhou 450001, People's Republic of China

^a Also at Bogazici University, 34342 Istanbul, Turkey

^b Also at the Moscow Institute of Physics and Technology, Moscow 141700, Russia

^c Also at the Novosibirsk State University, Novosibirsk, 630090, Russia

^d Also at the NRC "Kurchatov Institute", PNPI, 188300, Gatchina, Russia

^e Also at Istanbul Arel University, 34295 Istanbul, Turkey

^f Also at Goethe University Frankfurt, 60323 Frankfurt am Main, Germany

^g Also at Key Laboratory for Particle Physics, Astrophysics and Cosmology, Ministry of Education; Shanghai Key Laboratory for Particle Physics and Cosmology; Institute of Nuclear and Particle Physics, Shanghai 200240, People's Republic of China

^h Also at Key Laboratory of Nuclear Physics and Ion-beam Application (MOE) and Institute of Modern Physics, Fudan University, Shanghai 200443, People's Republic of China

ⁱ Also at Harvard University, Department of Physics, Cambridge, MA, 02138, USA

^j Currently at: Institute of Physics and Technology, Peace Ave.54B, Ulaanbaatar 13330, Mongolia

^k Also at State Key Laboratory of Nuclear Physics and Technology, Peking University, Beijing 100871, People's Republic of China

^l School of Physics and Electronics, Hunan University, Changsha 410082, China

^m Also at Guangdong Provincial Key Laboratory of Nuclear Science, Institute of Quantum Matter, South China Normal University, Guangzhou 510006, China

ⁿ Currently at: Institute of Modern Physics, Lanzhou 730000, People's Republic of China

Abstract

The electromagnetic process $e^+e^- \rightarrow p\bar{p}$ is studied with the initial-state-radiation technique using 7.5 fb^{-1} of data collected by the BESIII experiment at seven energy points from 3.773 to 4.600 GeV. The Born cross section and the effective form factor of the proton are measured from the production threshold to $3.0 \text{ GeV}/c^2$ using the $p\bar{p}$ invariant-mass spectrum. The ratio of electric and magnetic form factors of the proton is determined from the analysis of the proton-helicity angular distribution.

Keywords: proton, electromagnetic form factors, initial state radiation, BESIII

1. Introduction

The investigation of nucleon structure through electromagnetic probes plays a central role in the understanding of strong interactions. Space-like (SL) photons (momentum transfer squared $q^2 < 0$) in elastic

electron-nucleon scattering experiments allow an accurate description of the three-dimensional structure of the nucleon through the study of the electromagnetic form factors (FFs). The electric FF G_E and the magnetic FF G_M are assumed to be analytic functions of q^2 [1], and

thus are also defined for the time-like (TL) kinematic domain $q^2 > 0$. Furthermore, it is possible to relate SL and TL FFs through dispersion relations [2]. In the TL region, nucleon FFs can be associated with the time evolution of the charge and magnetic distributions inside the nucleon [3].

Compared to the SL sector, where a percent level precision has been achieved [4], the knowledge of the TL proton FF is rather limited. Proton FFs in the TL region have been studied by various experiments in the direct annihilation processes $e^+e^- \rightarrow p\bar{p}$ [5–16] and $p\bar{p} \rightarrow e^+e^-$ [17–20], and in the initial-state-radiation (ISR) process $e^+e^- \rightarrow p\bar{p}\gamma$ [21–24]. Due to low statistics, many previous experiments have only determined the absolute value of the effective FF of the proton from the cross-section measurement. More recent measurements [14, 15, 18, 21, 22] have been able to determine the ratio of the proton FF absolute values ($R_{\text{em}} = |G_{\text{E}}|/|G_{\text{M}}|$) in the $p\bar{p}$ invariant mass ($M_{p\bar{p}}$) region below $3.08 \text{ GeV}/c^2$. The best determination of R_{em} , with a precision of around 10%, has been achieved by BESIII [16].

The ISR technique with an undetected photon has been used in our previous study [24] of the process $e^+e^- \rightarrow p\bar{p}\gamma$ to measure the TL proton FFs. In that analysis, events were selected where the ISR photon was emitted at small polar angles (SA-ISR), and hence the threshold region below $2 \text{ GeV}/c$ was not accessible due to the limited angular acceptance of the BESIII tracking system. In this Letter we extend our previous study to the case where the ISR photon is emitted at large polar angles (LA-ISR) and is detected. This al-

lows access to the threshold region and provides measurements of the proton helicity angle θ_p in the full $M_{p\bar{p}}$ range, in contrast to the analysis of the SA-ISR events. By analyzing the distribution of θ_p , defined in the process $e^+e^- \rightarrow p\bar{p}\gamma$ as the angle between the proton momentum in the $p\bar{p}$ rest frame and the momentum of the $p\bar{p}$ system in the e^+e^- c.m. frame, it is possible to determine the ratio of the proton FFs.

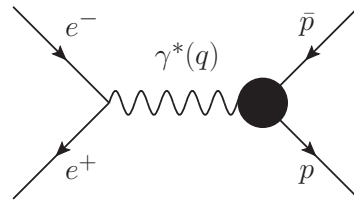


Figure 1: Feynman diagram for the process $e^+e^- \rightarrow p\bar{p}$ under the assumption of one virtual photon exchange. The bold vertex provides access to the hadronic FFs information.

In the e^+e^- center-of-mass (c.m.) frame, the differential cross section for the process $e^+e^- \rightarrow p\bar{p}$ under the assumption of one virtual photon exchange (Figure 1) is [25]:

$$\frac{d\sigma_{p\bar{p}}(q^2)}{d\cos\vartheta} = \frac{\pi\alpha^2\beta\mathcal{C}}{2q^2} \left[|G_{\text{M}}(q^2)|^2 (1 + \cos^2\vartheta) + \frac{|G_{\text{E}}(q^2)|^2}{\tau} \sin^2\vartheta \right], \quad (1)$$

where q^2 is equal to the square of the $p\bar{p}$ invariant mass $M_{p\bar{p}}$, $\alpha \approx \frac{1}{137}$ is the fine structure constant, $\beta = \sqrt{1 - 1/\tau}$ is the velocity of the proton with $\tau = q^2/4m_p^2$ and m_p the proton mass, and ϑ is the polar angle of the proton in the e^+e^- c.m. frame where the z-axis points along the direction of the positron momentum. The Coulomb factor $\mathcal{C} = \frac{y}{1-e^{-y}}$ with $y = \frac{\pi\alpha}{\beta}$ accounts for the electromagnetic interaction between the outgoing proton and antiproton [22, 26]. The cross section depends on the moduli of the magnetic and electric

FFs, which can be determined from the analysis of the proton angular distribution. The precise knowledge of the FFs in a wide kinematic region probes the transition region, from non-perturbative to perturbative QCD (pQCD).

By integrating the differential cross section (Eq. (1)), the total cross section for the process $e^+e^- \rightarrow p\bar{p}$ is obtained,

$$\sigma_{p\bar{p}}(q^2) = \frac{4\pi\alpha^2\beta\mathcal{C}}{3q^2} \left[|G_M|^2 + \frac{|G_E|^2}{2\tau} \right]. \quad (2)$$

An effective FF is introduced as a linear combination of $|G_M|^2$ and $|G_E|^2$,

$$|G_{\text{eff}}| = \sqrt{\frac{2\tau|G_M|^2 + |G_E|^2}{2\tau + 1}}, \quad (3)$$

which is equivalent to $|G_M|$ determined under the assumption of $|G_M| = |G_E|$. A complementary approach to study the $e^+e^- \rightarrow p\bar{p}$ process is provided by the ISR technique. This technique makes use of the emission of at least one high energy photon off the beam particles (Figure 2) which reduces the invariant mass of the $p\bar{p}$ system in the final state. The differential cross section for the ISR process is

$$\begin{aligned} \frac{d\sigma_{p\bar{p}\gamma}(q^2)}{dq^2} &= \frac{1}{s} W(s, x) \sigma_{p\bar{p}}(q^2), \\ W(s, x) &= \frac{\alpha}{\pi x} \left(\ln \frac{s}{m_e^2} - 1 \right) (2 - 2x + x^2), \\ x &= \frac{2E_\gamma^*}{\sqrt{s}} = 1 - \frac{q^2}{s}, \end{aligned} \quad (4)$$

where E_γ^* is the energy of the ISR photon in the e^+e^- c.m. frame, $W(s, x)$ [27] is the radiator function which gives the probability of ISR photon emission, and m_e and \sqrt{s} are the electron mass and the c.m. energy of the beams, respectively. In the study of the $e^+e^- \rightarrow p\bar{p}\gamma$ process, the cross section for the process $e^+e^- \rightarrow p\bar{p}$

and the ratio of the proton FFs can be measured over the full $M_{p\bar{p}}$ range from the $p\bar{p}$ threshold to \sqrt{s} .

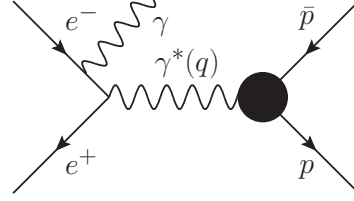


Figure 2: Lowest order Feynman diagram of the process $e^+e^- \rightarrow p\bar{p}\gamma$ assuming one virtual photon exchange, where γ is a real photon emitted from the initial state.

2. BESIII experiment and data sets

The BESIII experiment collects data at the BEPCII electron-positron collider, which operates at c.m. energies between $\sqrt{s} = 2.0$ and 4.7 GeV. The baryon TL FFs can be measured at BESIII both in ISR and in direct annihilation processes [28]. In this letter the investigation of the ISR process $e^+e^- \rightarrow p\bar{p}\gamma$ is reported. The data sets used in this analysis [29, 30] have been collected by BESIII at seven c.m. energies between 3.773 and 4.600 GeV with a total integrated luminosity of 7.5 fb⁻¹ (see Table 1).

The cylindrical BESIII detector [31] covers 93% of the 4π solid angle around the interaction point (IP), where the electron and positron beams collide at a small angle of 22 mrad. Beginning with the innermost component, BESIII consists of the following subdetectors: (1) a helium-based Main Drift Chamber (MDC) composed of 43 cylindrical layers coaxial with the beam pipe, (2) a Time-of-Flight system (TOF) consisting of 176 plastic scintillator counters in the barrel part, and 96 counters in the endcaps, (3) an Electro-Magnetic Calorimeter (EMC) consisting of a barrel and two endcaps with

6240 CsI(Tl) crystals, and (4) a Muon Counter (MUC) composed of nine Resistive Plate Chamber (RPC) layers in the barrel and eight RPC layers in each endcap. The MDC provides a momentum resolution of 0.5% for charged tracks with 1 GeV/c momentum and a spatial resolution of 135 μm . The resolution of the energy-loss measurement (dE/dx) by the MDC is better than 6%. The time resolution of the TOF is 80 ps in the barrel and 110 ps in the endcaps. The EMC provides an energy measurement with a resolution of 2.5% in the barrel and 5% in the endcaps for photons/electrons with an energy of 1 GeV. The MUC is used to identify muons and provides a spatial resolution better than 2 cm. The MUC is housed in the return yoke of the solenoidal magnet, which provides 1 T magnetic field.

Monte Carlo (MC) signal and background samples, simulated using the GEANT4-based [32, 33] BESIII OBJECT ORIENTED SIMULATION TOOL (BOOST) software [34], are used to optimize the event selection criteria, estimate the background contamination and determine the selection efficiency. The signal process $e^+e^- \rightarrow p\bar{p}\gamma$ is generated with the event generator PHOKHARA 9.1 [35], which includes radiative corrections of ISR up to next-to-leading order, final-state-radiation and vacuum polarization. Inclusive MC samples generated with BesEvtGen event generator [36] are used to simulate all the hadronic final states containing u , d and s quarks. The dominant background channel, $e^+e^- \rightarrow p\bar{p}\pi^0$, is generated exclusively using the phase space CONEXC [36] generator.

Table 1: The integrated luminosity \mathcal{L} of the data sets used in the $e^+e^- \rightarrow p\bar{p}\gamma$ analysis. The uncertainties are statistical and systematic, respectively.

\sqrt{s} [GeV]	\mathcal{L} [pb^{-1}]
3.773	$2931.8 \pm 0.2 \pm 13.8$ [29]
4.009	$481.96 \pm 0.01 \pm 4.68$ [30]
4.230	$1053.9 \pm 0.1 \pm 7.0$ [30]
4.260	$825.67 \pm 0.13 \pm 8.01$ [30]
4.360	$539.84 \pm 0.10 \pm 5.24$ [30]
4.420	$1041.3 \pm 0.1 \pm 6.9$ [30]
4.600	$585.4 \pm 0.1 \pm 3.9$ [30]

3. Selection of $e^+e^- \rightarrow p\bar{p}\gamma$ events

Two charged tracks with net charge zero are required in the MDC. The point of closest approach to the IP for each of the tracks is required to lie within a 1 cm radius in the plane perpendicular to the beam and ± 10 cm along the beam direction. The polar angle of the track with respect to the direction of the positron beam, θ , must be inside in the fiducial volume of the MDC, $|\cos\theta| < 0.93$. The particle identification (PID) from the relevant sub-detectors is combined to calculate probabilities for the pion, kaon, proton, electron and muon hypotheses for the tracks. The two charged tracks must be identified as a proton and an antiproton. In addition, the ratio E/p , with the energy E measured in the EMC and the momentum p measured in the MDC, is required to be smaller than 0.5 for the proton candidate to suppress the ISR Bhabha background. Photon candidates are selected using the information on the electromagnetic showers in the EMC. It is required that

the shower time is within 700 ns of the event start time to suppress electronic noise and energy deposits unrelated to the event. A photon candidate is selected if its deposited energy is greater than 25 MeV (50 MeV) in the barrel (endcap) region. The barrel (endcap) region is defined as $|\cos \theta_\gamma^*| < 0.80$ ($0.86 < |\cos \theta_\gamma^*| < 0.92$), where θ_γ^* is the photon polar angle. At least one high energy photon is required in the EMC with deposited energy higher than 0.4 GeV. The highest energy photon is then assumed to be the ISR photon candidate.

After the event reconstruction, a four-constraint (4C) kinematic fit is performed requiring the four-momentum conservation between the initial e^+e^- system and the final $p\bar{p}\gamma$ system. Events are selected as $e^+e^- \rightarrow p\bar{p}\gamma$ candidates if they fulfill the requirement $\chi_{4C}^2 < 50$. The background from the process $e^+e^- \rightarrow p\bar{p}\pi^0$ can not be completely removed by means of the kinematic fitting, and a dedicated background evaluation is performed, as described in the next section.

Figure 3 shows the combined $M_{p\bar{p}}$ spectrum for $p\bar{p}\gamma$ candidates selected at the seven energy points. The residual $e^+e^- \rightarrow p\bar{p}\pi^0$ background discussed in Section 4 is also shown (blue histogram in Figure 3). A clear peak from the resonance decay of $J/\psi \rightarrow p\bar{p}$ is seen in the spectrum. By fitting the J/ψ peak using a Breit-Wigner function convolved with a Gaussian, the number of resonance decays $J/\psi \rightarrow p\bar{p}$ ($N_{J/\psi}$) for each data sample is determined. The branching fraction $J/\psi \rightarrow p\bar{p}$ can be calculated for each data sample

individually as follows [37]:

$$\Gamma_{e^+e^-} \times \mathcal{B}(J/\psi \rightarrow p\bar{p}) = \frac{s m_{J/\psi}}{12\pi^2} \frac{N_{J/\psi}}{\epsilon_{J/\psi} W(s, x_{J/\psi}) \mathcal{L}}, \quad (5)$$

where $m_{J/\psi}$ is the mass of the resonance, $W(s, x_{J/\psi})$ is the radiator function ($x_{J/\psi} = 1 - M_{J/\psi}^2/s$), $\Gamma_{e^+e^-}$ is the electronic width of the J/ψ [38] and \mathcal{L} is the integrated luminosity collected at the given c.m. energy \sqrt{s} . The detection efficiency $\epsilon_{J/\psi}$ is determined from the signal MC simulations in the $M_{p\bar{p}}$ interval around the J/ψ resonance. The average value of $\mathcal{B}(J/\psi \rightarrow p\bar{p})$ obtained is $(2.13 \pm 0.09) \times 10^{-3}$, where the uncertainty is statistical only. This result is in a good agreement with the PDG value, $(2.12 \pm 0.03) \times 10^{-3}$ [38].

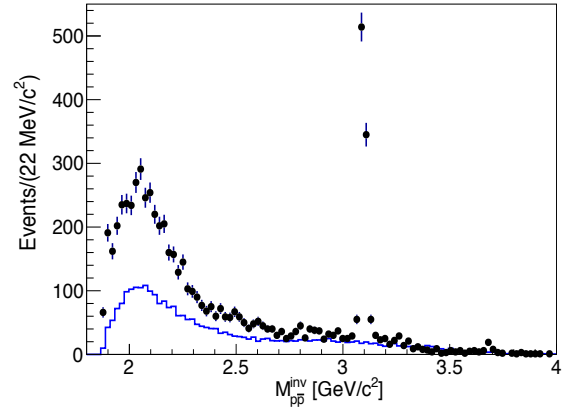


Figure 3: The $M_{p\bar{p}}$ spectrum for the full data sets (black dots with error bars), and the remaining $e^+e^- \rightarrow p\bar{p}\pi^0$ background (blue histogram).

4. Background estimation

For the processes $e^+e^- \rightarrow \pi^+\pi^-\gamma$, $K^+K^-\gamma$, $e^+e^-\gamma$ and $\mu^+\mu^-\gamma$ no MC events survive the selection cuts described in Section 3. The residual background

from these sources can be neglected, given the number of generated MC event exceeds the number of events expected in data.

The main source of background for the process under study is $e^+e^- \rightarrow p\bar{p}\pi^0$. To ensure a good description of this background in the simulation, the MC distributions of $M_{p\bar{p}}$ and $\cos\theta_p$ for the background process $e^+e^- \rightarrow p\bar{p}\pi^0$ are corrected by selecting data samples containing only the high-purity $p\bar{p}\pi^0$ final state. The $p\bar{p}\pi^0$ event selection uses the same criteria as the signal selection for the charged tracks and requires at least two photons in the EMC without the minimum energy cut of 0.4 GeV. After imposing the selection criteria for the charged tracks and photons, a five-constraint (5C) kinematic fit is performed for the $e^+e^- \rightarrow p\bar{p}\gamma\gamma$ hypothesis with requirements of energy and momentum conservation and the invariant mass of the two photon candidates being constrained to the π^0 mass [38]. The value of χ_{5C}^2 is required to be less than 60. To reject $p\bar{p}\gamma$ events, a 4C kinematic fit is performed to the proton, antiproton and the highest energy photon. The value of χ_{4C}^2 is required to be larger than 25. This selection provides a clean $p\bar{p}\pi^0$ event sample with the $e^+e^- \rightarrow p\bar{p}\gamma$ contamination below 0.1% level, as estimated from the MC simulation. To calculate the remaining $p\bar{p}\pi^0$ background contamination in the selected $p\bar{p}\gamma$ signal candidates, a weighting method is applied:

$$\mathcal{N}^{\text{bkg}} = \mathcal{N}_{\pi^0}^{\text{dat}} \times \frac{\mathcal{N}_{\text{isr}}^{\text{MC}}}{\mathcal{N}_{\pi^0}^{\text{MC}}}, \quad (6)$$

where \mathcal{N}^{bkg} is the estimated number of remaining $p\bar{p}\pi^0$ background events, $\mathcal{N}_{\pi^0}^{\text{dat}}$ and $\mathcal{N}_{\pi^0}^{\text{MC}}$ are the numbers of $p\bar{p}\pi^0$ events selected from data and $p\bar{p}\pi^0$ MC samples,

respectively, and $\mathcal{N}_{\text{isr}}^{\text{MC}}$ is the number of events selected as $p\bar{p}\gamma$ from the $p\bar{p}\pi^0$ MC samples.

The background estimate \mathcal{N}^{bkg} is calculated in two-dimensional intervals of $\cos\theta_p$ and $M_{p\bar{p}}$ distributions used for the determination of R_{em} . For the determination of the Born cross section for the process $e^+e^- \rightarrow p\bar{p}$, \mathcal{N}^{bkg} is calculated in intervals of $M_{p\bar{p}}$. The distribution of \mathcal{N}^{bkg} as a function of $M_{p\bar{p}}$, summed over the seven c.m. energy points, is shown as the blue histogram in Figure 3.

5. Ratio of proton form factors

The ratio of the electric and magnetic FFs R_{em} is determined by analyzing the distribution of $\cos\theta_p$

$$\frac{dN}{d\cos\theta_p} = \mathcal{A}[\mathcal{F}_{\text{M}}(\cos\theta_p, M_{p\bar{p}}) + \frac{R_{\text{em}}^2}{2\tau} \mathcal{F}_{\text{E}}(\cos\theta_p, M_{p\bar{p}})], \quad (7)$$

where N is the number of selected $e^+e^- \rightarrow p\bar{p}\gamma$ candidates after $e^+e^- \rightarrow p\bar{p}\pi^0$ background subtraction. The shapes of the magnetic contribution $\mathcal{F}_{\text{M}}(\cos\theta_p, M_{p\bar{p}})$ and the electric contribution $\mathcal{F}_{\text{E}}(\cos\theta_p, M_{p\bar{p}})$ are determined from the MC simulation, which includes the radiative corrections. The distributions obtained for \mathcal{F}_{M} and \mathcal{F}_{E} in a given $M_{p\bar{p}}$ interval are approximately proportional to $1 + \cos^2\theta_p$ and $\sin^2\theta_p$, respectively, as follows from Eq. (1). The factor $\frac{1}{2}$ arises from the normalization of \mathcal{F}_{M} and \mathcal{F}_{E} to the same integral, and the parameter \mathcal{A} is an overall normalization factor. In the fit function, τ is calculated as the mean value over the $p\bar{p}$ mass interval.

The ratio of the proton FFs is determined by fitting the $\cos\theta_p$ distribution in six $M_{p\bar{p}}$ intervals from

threshold to $3.0 \text{ GeV}/c^2$, with $M_{p\bar{p}}$ reconstructed from the measured tracks of the proton and antiproton candidates. For each data set and $M_{p\bar{p}}$ interval, the estimated background from the process $e^+e^- \rightarrow p\bar{p}\pi^0$ is subtracted from the number of signal candidates. The remaining signal is corrected for the selection efficiency calculated with corresponding MC samples and the efficiency-corrected distributions from all data sets are combined. Figure 4 shows the $\cos\theta_p$ distribution for six $M_{p\bar{p}}$ intervals, and the results of the fits using Eq. (7). Table 2 summarizes the R_{em} ratios obtained from the fits.

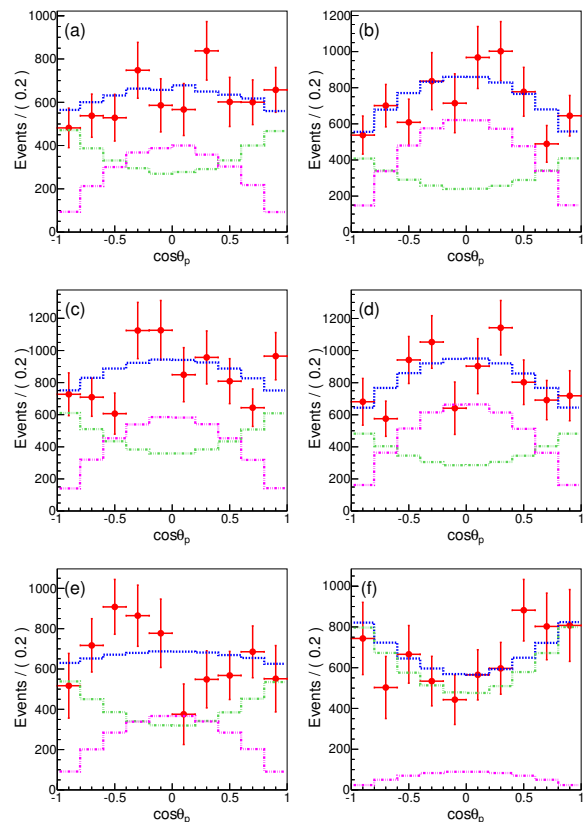


Figure 4: The efficiency-corrected $\cos\theta_p$ distribution for different $M_{p\bar{p}}$ intervals after combining all data sets, (a) threshold– $1.95 \text{ GeV}/c^2$, (b) $1.95\text{--}2.025 \text{ GeV}/c^2$, (c) $2.025\text{--}2.10 \text{ GeV}/c^2$, (d) $2.10\text{--}2.20 \text{ GeV}/c^2$, (e) $2.20\text{--}2.40 \text{ GeV}/c^2$ and (f) $2.40\text{--}3.00 \text{ GeV}/c^2$. The red dots represent the distribution from data after $e^+e^- \rightarrow p\bar{p}\pi^0$ background subtraction (as described in the text) and MC efficiency correction, the blue dotted lines show the fit to the data, and the green and purple dash-dotted histograms represent the magnetic and electric contributions to the fit, respectively.

Table 2: Sum of the numbers of selected $e^+e^- \rightarrow p\bar{p}\gamma$ candidates (\mathcal{N}_k) and the number of $e^+e^- \rightarrow p\bar{p}\pi^0$ background events ($\mathcal{N}_k^{\text{bkg}}$) over the seven c.m. energy points, and the results for the ratio R_{em} obtained from the fit for each $M_{p\bar{p}}$ interval k .

Mass Int. [GeV/c ²]	\mathcal{N}_k	$\mathcal{N}_k^{\text{bkg}}$	R_{em} ($ \mathcal{G}_{\text{E}} / \mathcal{G}_{\text{M}} $)
1.877-1.950	584	160±5	1.27± 0.23 ± 0.09
1.950-2.025	802	314±7	1.78± 0.33±0.11
2.025-2.100	912	352±8	1.46± 0.27 ± 0.09
2.100-2.200	905	370±8	1.82± 0.37± 0.24
2.200-2.400	929	477±9	1.36± 0.37 ±0.22
2.400-3.000	1159	656±10	0.64± 0.47 ± 0.22

The total systematic uncertainties for the measurement of the ratio of the proton FFs are listed in Table 2. The uncertainties include contributions from three main sources: the number of $\cos\theta_p$ intervals in the fit, the 4C-kinematic fit and the uncertainty of the $e^+e^- \rightarrow p\bar{p}\pi^0$ background estimation. The contribution from the number of $\cos\theta_p$ intervals is evaluated by using $\cos\theta_p$ distributions with eight intervals instead of ten. The variations of the fit results are taken as systematic uncertainties. The systematic uncertainty from the 4C-kinematic fit is caused by inconsistencies between χ_{4C}^2 distributions in data and simulation. It is estimated by modifying the helix parameters of the charged tracks for the MC samples according to the method described in Ref. [39]. Clean samples of selected $e^+e^- \rightarrow p\bar{p}\pi^0$ events are used to compare the χ_{4C}^2 distributions for data and MC simulation. The difference in the determined R_{em} with and without this modification is taken as the systematic uncertainty. To determine the uncertainty from the background estimation, the number of

background events obtained in Section 4 is varied by one standard deviation and the fit results after subtraction of the modified background are compared with the nominal values. Other contributions to the R_{em} systematic uncertainty are negligible, when compared to the size of the total uncertainty.

Figure 5 shows the results for R_{em} from this analysis (red points), together with the results from previous measurements. Both statistical and systematic uncertainties are included.

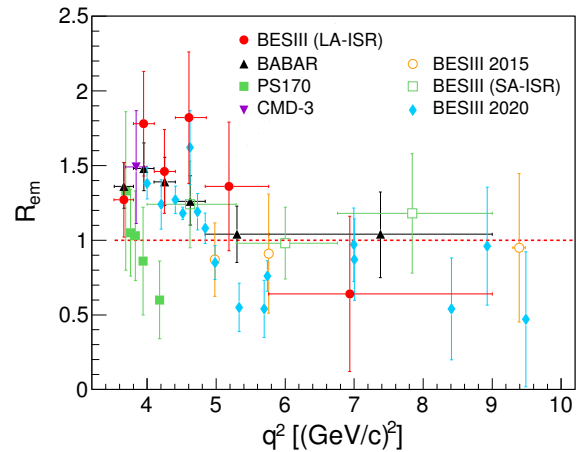


Figure 5: Results for R_{em} from this work (BESIII (LA-ISR), red solid dots) as a function of the momentum transfer squared, q^2 , together with the results from previous experiments: *BABAR* [22], PS170 [18], CMD-3 [15], and BESIII [14, 16, 24]. Both statistical and systematic uncertainties are included in all the results.

6. Cross section for the process $e^+e^- \rightarrow p\bar{p}$ and proton effective form factor

The Born cross section for the process $e^+e^- \rightarrow p\bar{p}$ is calculated in each $M_{p\bar{p}}$ interval i and for each data sample j ($j = 1, 2, \dots, 7$) as follows:

$$\sigma_{ij} = \frac{\mathcal{N}_{ij} - \mathcal{N}_{ij}^{\text{bkg}}}{\epsilon_{ij}(1 + \delta_{ij})\mathcal{L}_{ij}}, \quad (8)$$

where \mathcal{N}_{ij} is the number of selected $e^+e^- \rightarrow p\bar{p}\gamma$ candidates, $\mathcal{N}_{ij}^{\text{bkg}}$ is the number of $e^+e^- \rightarrow p\bar{p}\pi^0$ background events, ϵ_{ij} is the detection efficiency, $(1 + \delta_{ij})$ is the radiative correction factor calculated from the MC simulations and \mathcal{L}_{ij} is the ISR binned integrated luminosity. The index j runs over the seven c.m. energies. The binned integrated luminosity \mathcal{L}_{ij} is calculated as:

$$\mathcal{L}_{ij} = \int W(s_j, x_{ij}) \mathcal{L}_j dx_{ij}, \quad x_{ij} = 1 - \frac{q_{ij}^2}{s_j}, \quad (9)$$

where $W(s_j, x_{ij})$ [Eq. (4)] is a function of the c.m. energy squared s_j ($j = 1, 2, \dots, 7$) and the energy fraction x_{ij} , and \mathcal{L}_j is the integrated luminosity collected at the c.m. energy $\sqrt{s_j}$ (Table 1). The integration in Eq. (9) is performed over the width of the selected $M_{p\bar{p}}$ interval. The sum over the seven energy points for the binned integrated luminosity (\mathcal{L}_i), the selected $e^+e^- \rightarrow p\bar{p}\gamma$ candidates (\mathcal{N}_i) and the background events ($\mathcal{N}_i^{\text{bkg}}$) in each $M_{p\bar{p}}$ interval is given in Table 4. The averages over the seven c.m. energy points of the selection efficiencies ($\bar{\epsilon}_i$) and the radiative correction factors ($\overline{(1 + \delta_i)}$) calculated as:

$$\begin{aligned} \bar{\epsilon}_i &= \Sigma_j(\epsilon_{ij} \mathcal{L}_{ij}) / \mathcal{L}_i, \\ \overline{(1 + \delta_i)} &= \Sigma_j((1 + \delta_{ij}) \mathcal{L}_{ij}) / \mathcal{L}_i, \end{aligned} \quad (10)$$

are also listed in Table 4. The Born cross sections σ_{ij} are combined using the method of simple weighted averages [40]:

$$\begin{aligned} \sigma_{p\bar{p}}(M_{p\bar{p}}) &= \sigma_i = \Sigma_j(w_{ij} \sigma_{ij}), \quad \Delta\sigma_i = \sqrt{\frac{1}{\Sigma_j W_{ij}}}, \\ w_{ij} &= \frac{W_{ij}}{\Sigma_l W_{il}}, \quad W_{ij} = \frac{1}{(\Delta\sigma_{ij})^2}, \end{aligned} \quad (11)$$

where $\Delta\sigma$ is the statistical uncertainty of the cross section σ . The indices j and l run over the seven c.m. en-

ergies. The systematic on the measurements of σ_{ij} at the different c.m. energies are fully correlated and therefore need not be considered when determining the combination. The effective FF of the proton is calculated according to Eqs. (2) and (3).

The experimental resolution on $M_{p\bar{p}}$ is typically eight times smaller than the width of $M_{p\bar{p}}$ intervals and the event migration across the intervals is relatively small, well below the total uncertainty of the measured cross sections. The migration effect is taken into account using the MC simulation.

Several sources are considered as contributing to the systematic uncertainties. The uncertainties from tracking and PID efficiencies and the E/p requirement are each 1.0% per track for all the $p\bar{p}$ mass intervals [14]. The systematic uncertainty of the luminosity measurement is 1.0% for all the data sets [29, 30]. The systematic uncertainties due to the 4C-kinematic fit and the background estimation are determined using the same methods as described in Section 5. The radiative correction factor $(1 + \delta)$ is calculated in PHOKHARA generator with a theoretical uncertainty of 1%. The uncertainty from the energy dependence of the Born cross section used for the $(1 + \delta)$ calculation is determined by varying the line shape of the cross section from PHOKHARA event generator within the errors of the measured cross section. The systematic uncertainties listed above are added in quadrature and are summarized in Table 3.

In Table 4, the obtained values of the Born cross section for the process $e^+e^- \rightarrow p\bar{p}$ and the effective FF of the proton are listed including the statistical and systematic uncertainties. Figures 6a and 6b show the

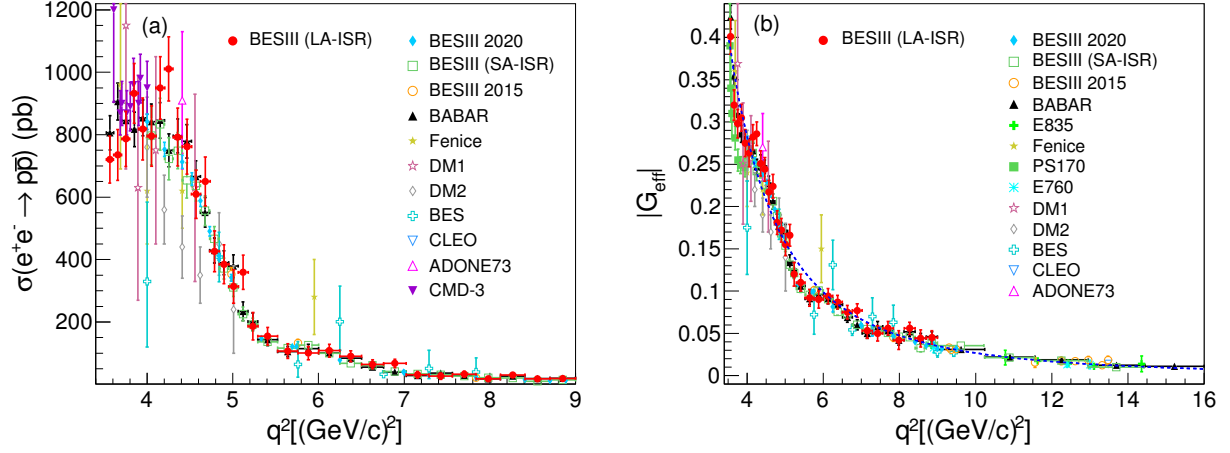


Figure 6: The cross section for the process $e^+e^- \rightarrow p\bar{p}$ (a) and the effective FF of the proton (b) measured in this work (red points), together with the results from previous experiments: BESIII [14, 16, 24], *BABAR* [22, 23], E835 [19, 20], Fenice [9–11], PS170 [18], E760 [17], DM1 [6], DM2 [7, 8], BES [13], CLEO [12], and ADONE73 [5]. The blue dashed curve shows the parameterization from Ref. [41] based on Eq. (12).

results from this analysis for the $e^+e^- \rightarrow p\bar{p}$ cross section and the proton effective FF, respectively, together with results from previous experiments.

Table 3: Summary of the systematic uncertainty contributions (in %) to the measurement of the Born cross section for the process $e^+e^- \rightarrow p\bar{p}$. The contributions from the tracking and PID efficiencies, E/p requirement, radiative corrections and luminosity are uniform over the considered $p\bar{p}$ mass range. The systematic uncertainty due to the 4C kinematic fit and background subtraction depends on the $p\bar{p}$ mass interval. The systematic uncertainties are added in quadrature (last row of the table).

Source	Uncertainty (%)
Tracking efficiency	2
PID efficiency	2
E/p	1
Luminosity	1
Radiative corrections	1 - 4
4C kinematic fit	1 - 4
Background subtraction	1 - 8
Sum (cross section)	4 - 9

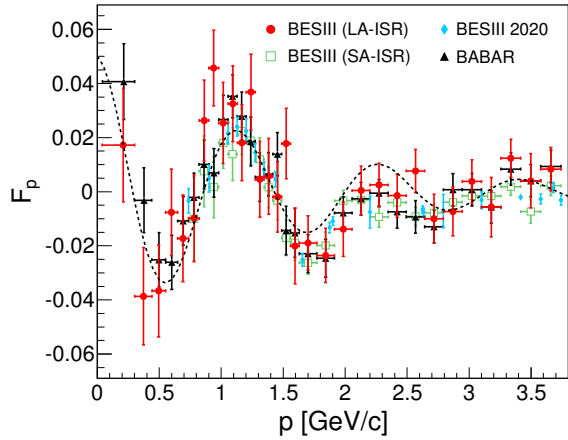


Figure 7: The effective FF of the proton, after subtraction of the smooth function described by Eq. (12), as a function of the relative momentum p . The data are from the present analysis (red points) and previous measurements of BESIII [16, 24] and *BABAR* [22, 23]. The black dashed curve shows the parameterization from Ref. [42] based on Eq. (13).

The data on the TL effective FF are best reproduced by the function proposed in Ref. [41],

$$|G_{\text{eff}}| = \frac{\mathcal{A}}{(1 + q^2/m_a^2)[1 - q^2/q_0^2]^2}, \quad q_0^2 = 0.71 \text{ (GeV}/c)^2, \quad (12)$$

where $\mathcal{A} = 7.7$ and $m_a^2 = 14.8 \text{ (GeV}/c)^2$ are the fit parameters obtained previously in Ref. [43]. This function is illustrated in Fig. 6b by the blue dashed curve and reproduces the behavior of the effective FF over the full q^2 range. However, the measurements indicate oscillating structures which are clearly seen when the residuals are plotted as a function of the relative momentum p of the final proton and antiproton [42]. Figure 7 shows the values of the proton effective FF as a function of p after subtraction of the smooth function described by Eq. (12). The black curve in Fig. 7 describes the peri-

odic oscillations and has the form [42]

$$F_p = A^{\text{osc}} \exp(-B^{\text{osc}} p) \cos(C^{\text{osc}} p + D^{\text{osc}}), \quad (13)$$

where $A^{\text{osc}} = 0.05$, $B^{\text{osc}} = 0.7 \text{ (GeV}/c)^{-1}$, $C^{\text{osc}} = 5.5 \text{ (GeV}/c)^{-1}$ and $D^{\text{osc}} = 0.0$ have been obtained from a fit to the *BABAR* data [43].

7. Summary

Using seven data sets with a total integrated luminosity of 7.5 fb^{-1} collected by the BESIII experiment at \sqrt{s} between 3.773 and 4.600 GeV, the ratio of the proton electromagnetic FF absolute values, the Born cross section for the process $e^+e^- \rightarrow p\bar{p}$ and the effective FF of the proton are measured from the $p\bar{p}$ threshold to $3.0 \text{ GeV}/c^2$ through the ISR process $e^+e^- \rightarrow p\bar{p}\gamma$. This measurement confirms an enhancement of the ratio of FFs in the $M_{p\bar{p}}$ region below $2.2 \text{ GeV}/c^2$ previously observed by *BABAR* and BESIII and differs from the behavior reported by PS170 [18]. Close to the threshold, the observed ratio is compatible with unity within the uncertainties. The results on the Born cross section for the process $e^+e^- \rightarrow p\bar{p}$ and the proton effective FF presented in this work are in a good agreement with the measurements from the previous experiments [5–22, 24]. In particular, we reproduce the structures seen in the *BABAR* and previous BESIII measurements of the proton effective FF. The origin of these oscillating structures can be attributed to an interference effect involving rescattering processes in the final state [43] or to independent resonant structures, as in Ref. [44]. The precision of the measurements obtained in this work are comparable to or lower than that achieved in previous

Table 4: The integrated luminosity (\mathcal{L}_i), the number of candidates (\mathcal{N}_i), the estimated $e^+e^- \rightarrow p\bar{p}\pi^0$ background ($\mathcal{N}_i^{\text{bkg}}$), the average over the seven c.m. energy points of the selection efficiencies ($\bar{\epsilon}_i$) and the radiative correction factors ($\overline{(1 + \delta_i)}$), the measured $e^+e^- \rightarrow p\bar{p}$ Born cross section (σ_i) and the effective FF ($|G_{\text{eff}}|$).

$M_{p\bar{p}}$ [GeV/ c^2]	\mathcal{L}_i [pb $^{-1}$]	\mathcal{N}_i	$\mathcal{N}_i^{\text{bkg}}$	$\bar{\epsilon}_i$	$\overline{(1 + \delta_i)}$	σ_i [pb]	$ G_{\text{eff}} $
1.877 - 1.900	2.11	167	30.8 ± 2.3	0.071	1.21	$721 \pm 71 \pm 26$	$0.401 \pm 0.020 \pm 0.007$
1.900 - 1.925	2.30	194	52.8 ± 3.0	0.068	1.15	$735 \pm 77 \pm 26$	$0.320 \pm 0.017 \pm 0.006$
1.925 - 1.950	2.36	223	77.4 ± 3.6	0.069	1.13	$787 \pm 84 \pm 30$	$0.298 \pm 0.016 \pm 0.006$
1.950 - 1.975	2.41	263	88.8 ± 3.9	0.068	1.12	$933 \pm 90 \pm 34$	$0.305 \pm 0.015 \pm 0.006$
1.975 - 2.000	2.47	270	113.0 ± 4.4	0.067	1.12	$818 \pm 90 \pm 41$	$0.275 \pm 0.015 \pm 0.007$
2.000 - 2.025	2.53	269	114.6 ± 4.4	0.067	1.11	$796 \pm 89 \pm 38$	$0.263 \pm 0.015 \pm 0.006$
2.025 - 2.050	2.59	309	118.9 ± 4.5	0.066	1.11	$950 \pm 93 \pm 38$	$0.282 \pm 0.014 \pm 0.006$
2.050 - 2.075	2.65	321	123.1 ± 4.6	0.066	1.11	$1011 \pm 95 \pm 41$	$0.286 \pm 0.013 \pm 0.006$
2.075 - 2.100	2.72	282	112.8 ± 4.4	0.065	1.11	$792 \pm 86 \pm 36$	$0.251 \pm 0.014 \pm 0.006$
2.100 - 2.125	2.79	264	105.7 ± 4.2	0.066	1.10	$762 \pm 82 \pm 31$	$0.244 \pm 0.013 \pm 0.005$
2.125 - 2.150	2.85	227	92.7 ± 3.9	0.066	1.10	$610 \pm 73 \pm 25$	$0.217 \pm 0.013 \pm 0.004$
2.150 - 2.175	2.93	236	92.4 ± 3.9	0.065	1.10	$650 \pm 74 \pm 26$	$0.224 \pm 0.013 \pm 0.004$
2.175 - 2.200	3.00	178	81.2 ± 3.7	0.066	1.10	$427 \pm 62 \pm 19$	$0.181 \pm 0.013 \pm 0.004$
2.200 - 2.225	3.08	174	83.7 ± 3.7	0.066	1.10	$385 \pm 60 \pm 17$	$0.172 \pm 0.013 \pm 0.004$
2.225 - 2.250	3.15	140	65.2 ± 3.3	0.067	1.10	$314 \pm 52 \pm 14$	$0.155 \pm 0.013 \pm 0.003$
2.250 - 2.275	3.24	152	65.4 ± 3.3	0.068	1.10	$359 \pm 53 \pm 15$	$0.166 \pm 0.012 \pm 0.004$
2.275 - 2.300	3.32	114	62.1 ± 3.2	0.068	1.09	$186 \pm 43 \pm 11$	$0.120 \pm 0.014 \pm 0.003$
2.300 - 2.350	6.91	192	105.6 ± 4.2	0.070	1.10	$154 \pm 27 \pm 8$	$0.110 \pm 0.010 \pm 0.003$
2.350 - 2.400	7.28	157	93.5 ± 3.9	0.072	1.09	$107 \pm 23 \pm 6$	$0.092 \pm 0.010 \pm 0.003$
2.400 - 2.450	7.69	149	82.1 ± 3.7	0.073	1.09	$100 \pm 20 \pm 8$	$0.090 \pm 0.009 \pm 0.003$
2.450 - 2.500	8.13	139	66.9 ± 3.3	0.075	1.08	$108 \pm 19 \pm 7$	$0.094 \pm 0.008 \pm 0.003$
2.500 - 2.550	8.60	126	62.8 ± 3.2	0.076	1.09	$90 \pm 17 \pm 5$	$0.087 \pm 0.008 \pm 0.002$
2.550 - 2.600	9.12	104	54.0 ± 3.0	0.077	1.08	$64 \pm 14 \pm 3$	$0.075 \pm 0.008 \pm 0.002$
2.600 - 2.650	9.68	109	52.9 ± 2.9	0.077	1.09	$67 \pm 13 \pm 3$	$0.077 \pm 0.008 \pm 0.002$
2.650 - 2.700	10.29	75	47.3 ± 2.8	0.078	1.08	$31 \pm 11 \pm 2$	$0.053 \pm 0.009 \pm 0.001$
2.700 - 2.750	10.97	73	47.4 ± 2.8	0.080	1.07	$26 \pm 10 \pm 2$	$0.050 \pm 0.009 \pm 0.002$
2.750 - 2.800	11.71	82	48.4 ± 2.8	0.080	1.07	$33 \pm 10 \pm 2$	$0.056 \pm 0.008 \pm 0.002$
2.800 - 2.850	12.54	70	50.6 ± 2.8	0.080	1.08	$18 \pm 9 \pm 1$	$0.042 \pm 0.011 \pm 0.002$
2.850 - 2.900	13.45	92	47.5 ± 2.7	0.080	1.06	$30 \pm 8 \pm 3$	$0.056 \pm 0.007 \pm 0.002$
2.900 - 2.950	14.47	69	49.9 ± 2.8	0.081	1.07	$18 \pm 8 \pm 1$	$0.044 \pm 0.010 \pm 0.002$
2.950 - 3.000	15.62	71	49.3 ± 2.8	0.082	1.06	$19 \pm 7 \pm 1$	$0.045 \pm 0.008 \pm 0.001$

BESIII studies [14, 16, 24] using the direct annihilation and SA-ISR processes which benefit from higher statistics. The analysis described here shows the possibility to use the LA-ISR technique at BESIII to perform independent and complementary measurements of the proton FFs down to the production threshold. Larger samples that are currently being collected by BESIII [28] will enhance the precision of these measurements.

Acknowledgement

The BESIII collaboration thanks the staff of BEPCII and the IHEP computing center for their strong support. This work is supported in part by National Natural Science Foundation of China (NSFC) under Contracts Nos. 11625523, 11635010, 11735014, 11822506, 11835012, 11935015, 11935016, 11935018, 11961141012; the Chinese Academy of Sciences (CAS) Large-Scale Scientific Facility Program; Joint Large-Scale Scientific Facility Funds of the NSFC and CAS under Contracts Nos. U1732263, U1832207; CAS Key Research Program of Frontier Sciences under Contracts Nos. QYZDJ-SSW-SLH003, QYZDJ-SSW-SLH040; 100 Talents Program of CAS; INPAC and Shanghai Key Laboratory for Particle Physics and Cosmology; ERC under Contract No. 758462; German Research Foundation DFG under Contracts Nos. 443159800, Collaborative Research Center CRC 1044, FOR 2359, FOR 2359, GRK 214; Istituto Nazionale di Fisica Nucleare, Italy; Ministry of Development of Turkey under Contract No. DPT2006K-120470; National Science and Technology fund; Olle Engkvist Foundation under Contract No. 200-0605; STFC (United Kingdom); The Knut and Al-

ice Wallenberg Foundation (Sweden) under Contract No. 2016.0157; The Royal Society, UK under Contracts Nos. DH140054, DH160214; The Swedish Research Council; U. S. Department of Energy under Contracts Nos. DE-FG02-05ER41374, DE-SC-0012069.

References

- [1] S. Drell, F. Zachariasen, Proton Electromagnetic form Factors (first edition), Oxford University Press, Belfast, 1961.
- [2] M. Belushkin, H.-W. Hammer, U.-G. Meissner, Phys. Rev. C 75 (2007) 035202. arXiv:hep-ph/0608337, doi:10.1103/PhysRevC.75.035202.
- [3] E. A. Kuraev, E. Tomasi-Gustafsson, A. Dbeysy, Phys. Lett. B 712 (2012) 240–244. doi:10.1016/j.physletb.2012.04.073.
- [4] V. Punjabi, C. Perdrisat, M. Jones, E. Brash, C. Carlson, Eur. Phys. J. A 51 (2015) 79. arXiv:1503.01452, doi:10.1140/epja/i2015-15079-x.
- [5] M. Castellano, G. Giugno, J. Humphrey, E. S. Palmieri, G. Troise, U. Troya, S. Vitale, Nuovo Cimento A 14 (1973) 1. doi:10.1007/BF02734600.
- [6] B. Delcourt, et al., Phys. Lett. B 86 (1979) 395–398. doi:10.1016/0370-2693(79)90864-5.
- [7] D. Bisello, et al., Nucl. Phys. B224 (1983) 379. doi:10.1016/0550-3213(83)90381-4.
- [8] D. Bisello, et al., Z. Phys. C 48 (1990) 23–28. doi:10.1007/BF01565602.
- [9] A. Antonelli, et al., Phys. Lett. B 313 (1993) 283–287. doi:10.1016/0370-2693(93)91225-C.
- [10] A. Antonelli, et al., Phys. Lett. B 334 (1994) 431–434. doi:10.1016/0370-2693(94)90710-2.
- [11] A. Antonelli, et al., Nucl. Phys. B 517 (1998) 3–35. doi:10.1016/S0550-3213(98)00083-2.
- [12] T. K. Pedlar, et al., Phys. Rev. Lett. 95 (2005) 261803. doi:10.1103/PhysRevLett.95.261803.
- [13] M. Ablikim, et al., Phys. Lett. B 630 (2005) 14–20. doi:10.1016/j.physletb.2005.09.044.
- [14] M. Ablikim, et al., Phys. Rev. D 91 (11) (2015) 112004. doi:10.1103/PhysRevD.91.112004.

- [15] R. R. Akhmetshin, et al., *Phys. Lett. B* 759 (2016) 634. doi:10.1016/j.physletb.2016.04.048.
- [16] M. Ablikim, et al., *Phys. Rev. Lett.* 124 (4) (2020) 042001. arXiv:1905.09001, doi:10.1103/PhysRevLett.124.042001.
- [17] T. A. Armstrong, et al., *Phys. Rev. Lett.* 70 (1993) 1212–1215. doi:10.1103/PhysRevLett.70.1212.
- [18] G. Bardin, et al., *Nucl. Phys. B* 411 (1994) 3–32. doi:10.1016/0550-3213(94)90052-3.
- [19] M. Ambrogiani, et al., *Phys. Rev. D* 60 (1999) 032002. doi:10.1103/PhysRevD.60.032002.
- [20] M. Andreotti, et al., *Phys. Lett. B* 559 (2003) 20–25. doi:10.1016/S0370-2693(03)00300-9.
- [21] B. Aubert, et al., *Phys. Rev. D* 73 (2006) 012005. arXiv:hep-ex/0512023, doi:10.1103/PhysRevD.73.012005.
- [22] J. P. Lees, et al., *Phys. Rev. D* 87 (9) (2013) 092005. doi:10.1103/PhysRevD.87.092005.
- [23] J. P. Lees, et al., *Phys. Rev. D* 88 (2013) 032011. doi:10.1103/PhysRevD.88.032011.
- [24] M. Ablikim, et al., *Phys. Rev. D* 99 (9) (2019) 092002. arXiv:1902.00665, doi:10.1103/PhysRevD.99.092002.
- [25] A. Zichichi, S. Berman, N. Cabibbo, R. Gatto, *Nuovo Cim.* 24 (1962) 170–180. doi:10.1007/BF02785769.
- [26] R. Baldini Ferroli, S. Pacetti, A. Zallo, *Eur. Phys. J. A* 48 (2012) 33. arXiv:1008.0542, doi:10.1140/epja/i2012-12033-6.
- [27] G. Bonneau, F. Martin, *Nucl. Phys. B* 27 (1971) 381. doi:10.1016/0550-3213(71)90102-7.
- [28] M. Ablikim, et al., *Chin. Phys. C* 44 (4) (2020) 040001. arXiv:1912.05983, doi:10.1088/1674-1137/44/4/040001.
- [29] M. Ablikim, et al., *Phys. Lett. B* 753 (2016) 629–638. doi:10.1016/j.physletb.2015.11.043.
- [30] M. Ablikim, et al., *Chin. Phys. C* 39 (2015) 093001. doi:10.1088/1674-1137/39/9/093001.
- [31] M. Ablikim, et al., *Nucl. Instrum. Methods Phys. Res., Sect. A* 614 (2010) 345. doi:10.1016/j.nima.2009.12.050.
- [32] S. Agostinelli, et al., *Nucl. Instrum. Methods Phys. Res., Sect. A* 1308 (2003) 250. doi:10.1016/S0168-9002(03)01368-8.
- [33] J. Allison, et al., *IEEE Trans. Nucl. Sci.* 53 (2006) 270. doi:10.1109/TNS.2006.869826.
- [34] Z. Y. Deng, et al., *Chin. Phys. C* 30 (2006) 371.
- [35] H. Czyz, J. H. Kuehn, S. Tracz, *Phys. Rev. D* 90 (2014) 114021. doi:10.1103/PhysRevD.90.114021.
- [36] R. G. Ping, et al., *Chin. Phys. C* 38 (2014) 083001. doi:10.1088/1674-1137/38/8/083001.
- [37] M. Benayoun, S. I. Eidelman, V. N. Ivanchenko, Z. K. Silagadze, *Mod. Phys. Lett. A* 14 (1999) 2605–2614. doi:10.1142/S021773239900273X.
- [38] C. Patrignani, et al., *Chin. Phys. C* 40 (10) (2016) 100001. doi:10.1088/1674-1137/40/10/100001.
- [39] M. Ablikim, et al., *Phys. Rev. D* 87 (1) (2013) 012002. arXiv:1208.4805, doi:10.1103/PhysRevD.87.012002.
- [40] M. Schmelling, *Phys. Scr.* 51 (6) (1995) 676. [link]. URL <http://stacks.iop.org/1402-4896/51/i=6/a=002>
- [41] E. Tomasi-Gustafsson, M. P. Rekaló, *Phys. Lett. B* 504 (2001) 291–295. doi:10.1016/S0370-2693(01)00312-4.
- [42] A. Bianconi, E. Tomasi-Gustafsson, *Phys. Rev. C* 93 (2016) 035201. doi:10.1103/PhysRevC.93.035201.
- [43] A. Bianconi, E. Tomasi-Gustafsson, *Phys. Rev. Lett.* 114 (23) (2015) 232301. doi:10.1103/PhysRevLett.114.232301.
- [44] I. T. Lorentz, H.-W. Hammer, U.-G. Meissner, *Phys. Rev. D* 92 (2015) 034018. doi:10.1103/PhysRevD.92.034018.